Acta Materialia 232 (2022) 117937

Contents lists available at ScienceDirect

Acta Materialia

journal homepage: www.elsevier.com/locate/actamat

Full length article

Dynamically reversible shear transformations in a CrMnFeCoNi high-entropy alloy at cryogenic temperature

Kaisheng Ming[a], Bo Li[a], Lichen Bai[a], Ping Jiang[b], Xiaolei Wu[b], Shijian Zheng[a,*], Jian Wang[c,*]

[a] State Key Laboratory of Reliability and Intelligence of Electrical Equipment, School of Materials Science and Engineering, Hebei University of Technology, Tianjin 300401, China
[b] State Key Laboratory of Nonlinear Mechanics, Institute of Mechanics, Chinese Academy of Sciences, Beijing 100190, China
[c] Mechanical and Materials Engineering, University of Nebraska-Lincoln, Lincoln, NE 68588, USA

ARTICLE INFO

Article history:
Received 24 February 2022
Revised 7 April 2022
Accepted 11 April 2022
Available online 12 April 2022

Keywords:
High-entropy alloy
Deformation twinning
Martensitic phase transformations
Mechanical properties
High-resolution electron microscope

ABSTRACT

Shear transformation, such as twinning and martensitic phase transformation, is generally unidirectional under monotonic thermal or mechanical loading. Here, we report the dynamically reversible shear transformations in a CrMnFeCoNi high-entropy alloy (HEA) under uniaxial tension at the extremely low temperature of 4.2 K. Since stacking fault energy (SFE) of CrMnFeCoNi HEA with a face-centered cubic (fcc) structure is low and decreases with decreasing temperature, plastic deformation is accommodated by dislocation slips and shear transformation bands, such as {111} stacking faults (SFs), {111} nano-twins and fcc → hcp (hexagonal close-packed structure) shear transformation bands. When deformed at 4.2 K, the lower SFE promotes fcc → hcp shear transformation, forming hcp grains. Besides basal and non-basal dislocation slips in hcp grains, high-density {0001} SFs and $\{10\bar{1}1\}$ nano-twinning are activated to accommodate plastic deformation. More intriguingly, reverse hcp → fcc shear transformations are stimulated by deformation-induced local dissipative heating. The reversible fcc ↔ hcp shear transformations and both $\{10\bar{1}1\}$ and {111} nano-twinning lead to dynamic nano-laminated dual-phase (NL-DP) structures, which advances the monotonic "dynamic Hall-Petch" effect in enhancing strength, strain-hardening ability, and ductility by dynamically tailoring the type and width of shear transformation bands. Our work provides a promising strategy for evading the strength-ductility dilemma via dynamically developing NL-DP structures through activating reversible shear transformations.

1. Introduction

Materials that dynamically develop characteristic microstructure to simultaneously improve strength, ductility, and strain-hardening ability are especially desirable since the strength and ductility of structural materials are generally mutually exclusive [1–4]. For example, twinning-induced plasticity steels and transformation-induced plasticity steels in which twinning or phase transformation not only contributes to plastic deformation, but also creates coherent twin/phase boundaries that strengthen materials by impeding dislocation motion and enhancing strain-hardening ability [5–8]. Such synergetic effect is referred to as the "dynamic Hall-Petch" effect associated with the development of hierarchical microstructure [9–11].

For high-entropy alloys (HEAs) with a face-centered cubic (fcc) structure, deformation-induced nano-twinning and/or fcc to hexagonal close-packed (hcp) phase transformation not only accommodates plastic deformation besides dislocation slips because of the low stacking fault energy (SFE) but also develops hierarchical nano-laminated structures which improve strength, strain-hardening capability, and ductility [12–25]. It is well known that the activity of twinning and fcc → hcp phase transformation is relying on the magnitude of the SFE of close-packed planes and the cohesive energy difference between fcc and hcp phases [26–28]. The SFE of fcc-phase CrMnFeCoNi HEAs decreases with decreasing temperature, and the temperature-dependent coefficient of SFE ($d\gamma/dT$) is approximately 0.09–0.11 mJ/m^2/K [29]. At deformation temperatures above 298 K, the SFE is greater than 20 mJ/m^2, and the plastic deformation is primarily accommodated by full dislocation slip [24,26]. At deformation temperatures in the ranges of 77–298 K, the SFE is in the range of 0 to 20 mJ/m^2, thus deformation twinning and Shockley partial dislocations act as major carriers for plasticity [24,26,30]. When the temperature is

* Corresponding authors.
E-mail addresses: sjzheng@hebut.edu.cn (S. Zheng), jianwang@unl.edu (J. Wang).

https://doi.org/10.1016/j.actamat.2022.117937
1359-6454/

further reduced below 77 K, the SFE is very small or even negative, and the cohesive energy for the hcp phase is close to or even lower than that for the fcc phase. Correspondingly, plastic deformation will be dominated by fcc → hcp shear transformation banding [26]. It must be pointed out that the fcc → hcp shear transformation is accommodated by successive gliding of Shockley partial dislocations on every two close-packed planes [28,31,32]. At cryogenic temperature, it is thus expected that the dominant fcc → hcp shear transformation mechanism will transform the initial fcc-phase grains to hcp-phase grains. The opening issue is how newly formed hcp grains plastically deform. The hcp materials generally generate various twins to accommodate the plastic deformation due to the insufficient independent slip systems. It has been reported that the deformation-induced reverse shear transformation (hcp → fcc) takes place at the junctions of two crossing hcp bands in FeMnCoCr HEA systems, which is triggered by the local dissipative heating and local complex stress fields [20,25]. Especially, does deformation-induced local dissipative heating affect deformation twinning behaviors of hcp phases at cryogenic temperature? Corresponding to the low SFE of the basal plane and local dissipative heating, we speculated that high-density basal stacking faults (SFs) can be generated, and then the local dissipative heating may promote shear transformation from hcp structure or basal SFs to fcc structures. Also, deformation twinning in the hcp phase may be activated to accommodate the ⟨c⟩ component of plastic strains besides dislocation slips. Furthermore, the local dissipative heating might facilitate the shear transformation from hcp twins to fcc structure. Thus, cryogenic temperature deformation may dynamically develop hierarchical dual-phase laminated structures associated with fcc → hcp, hcp→ twin in hcp, and hcp → fcc shear transformations, which can simultaneously enhance strength, ductility, and strain-hardening ability.

Here, we report the dynamically reversible fcc ↔ hcp shear transformations and deformation-induced dynamic nano-laminated dual-phase (NL-DP) structures in a single-phase fcc $Cr_{26}Mn_{20}Fe_{20}Co_{20}Ni_{14}$ HEA during tensile straining at 4.2 K. Extensive deformation-driven fcc → hcp shear transformations were promoted during tensile deformation at 4.2 K, leading to a large fraction of hcp grains. In addition to basal and non-basal slips in hcp grains, $\{10\bar{1}1\}$ twinning is activated to accommodate deformation in the ⟨c⟩ axis. More intriguingly, deformation-induced local dissipative heating at 4.2 K is sufficient to activate reverse shear transformation through two mechanisms: hcp → fcc shear transformation via nucleation and propagation of Shockley partial dislocations, and $\{10\bar{1}1\}$ twinning-assisted hcp → fcc shear transformation. Corresponding to the low temperature promoted fcc → hcp shear transformations and the local dissipative heating stimulated hcp → fcc reverse shear transformations, tensile deformation dynamically developed a hierarchical NL-DP structure, and the tensile stress-strain response exhibits serrated flow behavior at 4.2 K. Furthermore, we demonstrated that such NL-DP structures can simultaneously enhance the strength, strain-hardening capability, and ductility of $Cr_{26}Mn_{20}Fe_{20}Co_{20}Ni_{14}$ HEA at room temperature.

2. Experimental procedures

One Kg alloy ingot with nominal composition $Cr_{26}Mn_{20}Fe_{20}Co_{20}Ni_{14}$ (at.%) was fabricated by arc-melting under an argon atmosphere using pure metals (99.95 wt.% pure), subsequently homogenized in a vacuum at 1150 °C for 6 h and then cooled in the furnace. The homogenized ingot was forged into a slab of 10 mm in thickness at 1000 °C. The slab was then hot-rolled at 900 °C to the sheets with a thickness of 5 mm and cold-rolled to 3 mm in thickness with a reduction of 70%. Finally, the cold-rolled sheet was annealed at 1200 °C for 1 h, followed by air cooling. Microstructure characterizations were performed using a scanning electron microscope (TESCAN GAIA3) equipped with electron backscatter diffraction (EBSD). The samples for EBSD analysis were prepared by mechanical grinding, and polishing in a solution of 10% perchloric acid and 90% alcohol at −20 °C and an applied voltage of 20 V. The EBSD analysis reveals the initial fcc-phase, equiaxed grains with an average size of 150 μm (Fig. 1a, b).

Flat dog-bone-shaped tensile specimens (as shown in Fig. 2a) with a gage length of 15 mm, a thickness of 2 mm, and a width of 4 mm were machined from the annealed sheet by electric discharge machining with their longitudinal axes parallel to the rolling direction of the sheet. Then the tensile samples were ground to 1500-grit SiC paper before performing tensile testing. Tensile testing was performed at 4.2 K (liquid helium temperature), 77 K (liquid nitrogen temperature), and 298 K (room temperature) with the strain rates of 10^{-3} s^{-1} and 10^{-5} s^{-1} on an MTS-SANS CMT5000 universal testing machine. Microstructure characterizations at different deformation stages were performed using a JEM-

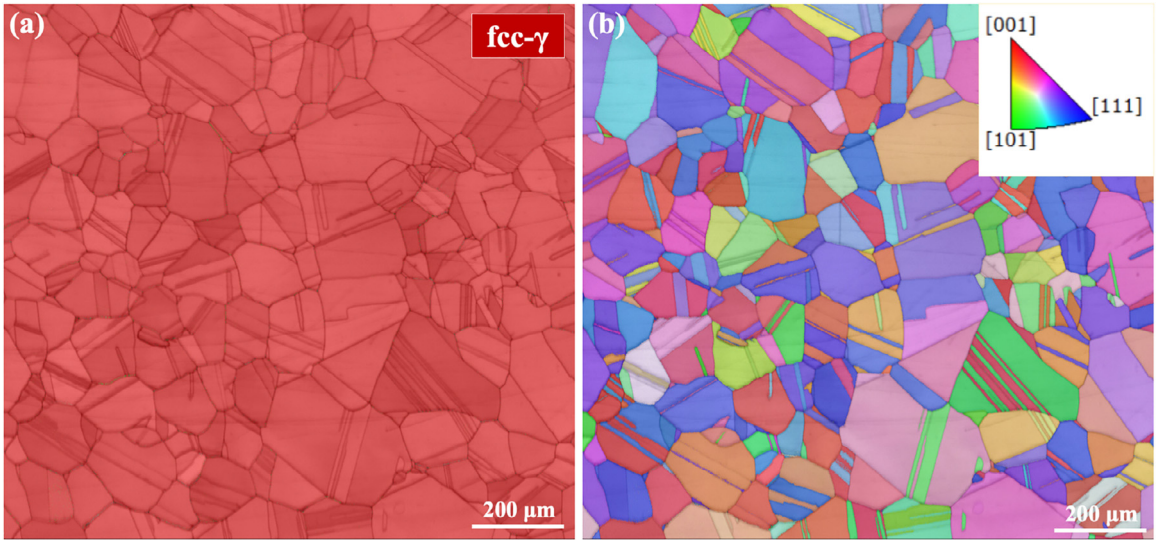

Fig. 1. Initial microstructure. (a) The EBSD phase map and (b) inverse pole figure map of the annealed $Cr_{26}Mn_{20}Fe_{20}Co_{20}Ni_{14}$ HEA before tensile testing, showing the single-phase fcc structure with fully recrystallized grains.

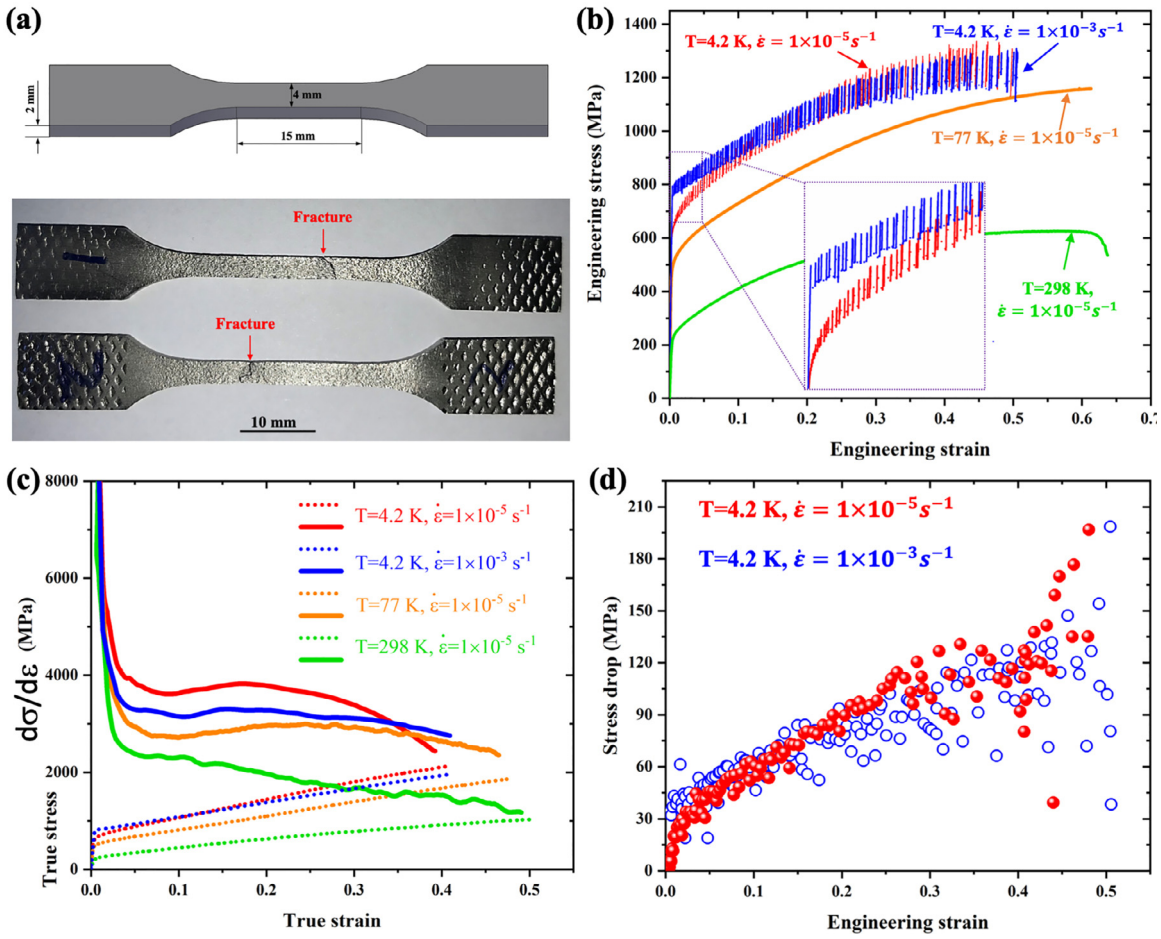

Fig. 2. Serrated flow behavior and exceptional mechanical properties. (a) Macroscopic images of tensile samples before and after tension to fracture at 4.2 K, showing uniform deformation without necking. (b) Representative tensile stress-strain curves at 4.2–298 K with the strain rates of 10^{-3} s^{-1} and 10^{-5} s^{-1}, with the enlarged section of stress-strain curves corresponding to yielding stage inset. (c) The corresponding true stress-strain curves (dashed lines) and strain-hardening curves (solid lines), showing the remarkable increase in strain-hardening rate with reducing testing temperatures. (d) The variation of the amplitude of stress drops with strain.

2100F transmission electron microscope (TEM) and JEM-ARM300F aberration-corrected scanning TEM (STEM). Specimens for TEM observation were extracted from the gage section of deformed specimens and then thinned using mechanical grinding followed by double-jet electro-polishing in a solution of 6% perchloric acid, 35% n–butyl alcohol, and 59% alcohol at 30 °C and an applied voltage of 30 V. Specimens for TEM observation were also made by grinding and polishing followed by low energy (3.5 keV) ion-milling (PIPS II System). All TEM samples were then cleaned by Solarus II Plasma Cleaner.

3. Results and discussion

3.1. Serrated flow behavior and exceptional mechanical properties at cryogenic temperature

Fig. 2b shows the representative tensile stress-strain curves of the single-phase fcc $Cr_{26}Mn_{20}Fe_{20}Co_{20}Ni_{14}$ HEA at 4.2–298 K with the strain rates ($\dot{\varepsilon}$) of 10^{-3} s^{-1} and 10^{-5} s^{-1}. Two intriguing plastic flow behaviors are observed. Firstly, pronounced serrated flow behavior extends from the initial yielding stage to the final fracture when the sample is stretched at 4.2 K, but not at 77 K and 298 K. The serrated behavior is characterized by periodically sudden stress drops and strain bursts. The amplitude of the stress drops increases with increasing strain, reaching up to a maximum value of ~198 MPa at the strains of 45%–50% (Fig. 2d). Second, lowering deformation temperature simultaneously increases the yield strength, ultimate tensile strength (Fig. 2b), and strain-hardening rate (Fig. 2c) without apparent loss of ductility. The macroscopic morphology of tensile samples after tension to fracture at 4.2 K indicates the uniform plastic deformation without necking (Fig. 2a). An exceptional combination of strength and ductility (yield strength of ~0.8 GPa, tensile strength of ~1.34 GPa as well as uniform elongation of ~50%) is realized at a deformation temperature of 4.2 K, which is much superior to that of the samples at deformation temperatures of 77 K and 298 K. In addition, such mechanical behaviors are insensitive to strain rate, although the yield strength increases with increasing strain rate (inset in Fig. 2b).

3.2. Deformation-induced lamellar dual-phase structures

For deformation at temperatures decreasing from 298 K to 77 K, the remarkable enhancement of strength, ductility, and strain-hardening rate of single-phase fcc HEAs are generally attributed to nano-twinning and/or fcc → hcp phase transformation [18,24,33,34], as shown in Fig. 3. Owing to the very low SFE of the current alloy, SFs mediate the initial plastic deformation at 298 K and 77 K (Fig. 3a_1, b_1). With increasing strains at 298 K, full dislocation slip dominates the plastic deformation instead of SFs, which gradually evolves into high-density dislocation walls due to the onset of dynamic recovery at high strains (Fig. 3a_2). In contrast, the dynamic recovery during deformation at 77 K can be impeded owing to the very low temperatures. The primary defor-

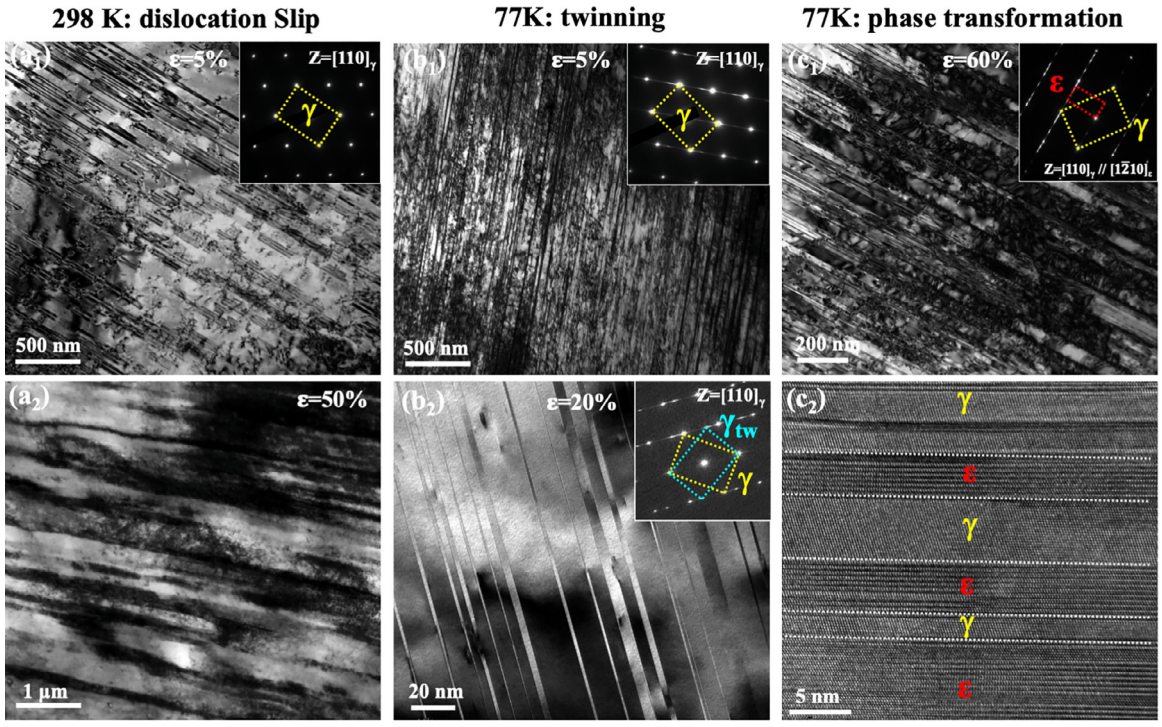

Fig. 3. The temperature-dependent deformation mechanisms in $Cr_{26}Mn_{20}Fe_{20}Co_{20}Ni_{14}$ HEA. TEM images of the samples after tensile deformation to (a_1) 5% and (a_2) 50% at 298 K, with the corresponding SADP inset, showing the formation of high-density of dislocation walls. TEM images of the samples after tensile deformation to (b_1) 5%, (b_2) 20%, and (b_3, b_4) 60% at 77 K, with corresponding SADPs inset, showing that the plastic deformation is primarily dominated by the motions of Shockley partial dislocations, and the corresponding formation of high-density of nano-twins (b_2) and fcc → hcp martensitic phase transformations (b_3, b_4).

mation mode is twining (Fig. 3b_1) and martensitic phase transformation (fcc → hcp) (Fig. 3c_1, c_2) at 77 K. For high-density of SFs, the faulted region can transform into either fcc structure or hcp structure through correcting SFs via nucleation and glide of Shockley partial dislocations, depending on the magnitude of SFE which corresponds to the energy difference between fcc and hcp structures [27,35,36]. Both twinning and phase transformation via nucleation and propagation of Shockley partial dislocations are energetically favorable because the process will reduce the density of SFs. Based on the TEM observation of microstructural evolutions during plastic deformation at 298 K and 77 K, the transition of deformation mechanisms from dislocation slips at 298 K to twinning and martensitic phase transformation at 77 K contributes to the enhanced mechanical properties with decreasing temperature. During plastic deformation, deformation-induced nano-twinning and phase transformation generate a high strain-hardening rate and remarkable increase in the tensile strength and ductility by continuously introducing coherent twin/phase boundaries that decrease the mean free path of dislocations ("dynamic Hall-Petch" effect) [9–11].

When deformation temperature is decreased to 4.2 K, the further enhancement in mechanical properties and the serrated flow behavior may involve additional micro-mechanical mechanisms of plastic deformation. After tension deformation to strains of 20% (Fig. 4a) and 50% (Fig. 4b), the color orientation contrast imaging (COCI) of the sample surfaces shows numerous parallel bands. Further microscopy characterizations reveal two types of laminated structures. An EBSD phase map (Fig. 4c) clearly shows one lamellar dual-phase structure where the fcc-γ and hcp-ε phases have an area fraction ratio of 11/9. It is noted that some bands are composed of two phases as indicated by arrows in Fig. 4c, implying the occurrence of local shear transformations inside hcp-ε or fcc-γ bands. We will characterize the corresponding mechanisms in the following section. The low-angle annular dark-field STEM (LAADF-STEM) imaging (Fig. 4d) shows the typical lamellar dual-phase structure, including high-density $\{10\bar{1}1\}$ nano-twins, {0001} SFs, {111} SFs, and fcc phase. $\{10\bar{1}1\}$ twins with an average thickness of ~20 nm display a much brighter contrast (positive strain contrast) than the surrounding hcp-ε matrix, suggesting severe lattice strain within twins. The corresponding selected-area diffraction pattern (SADP, in Fig. 4e) of the interface between the hcp-ε matrix and $\{10\bar{1}1\}$ twin shows two sets of diffraction spots corresponding to the fcc and hcp structures, evidencing the occurrence of hcp → fcc shear transformation inside/near $\{10\bar{1}1\}$ twins. The fcc phase formed in hcp domains is referred to as reversed fcc-γ. Note that the basal planes of the hcp-ε phase around the $\{10\bar{1}1\}$ twin are rotated slightly by ~5° as indicated in Fig. 4e.

A bright-field TEM image in Fig. 4f shows another type of lamellar dual-phase structure. The corresponding SADP, taken along the $[110]_\gamma$ zone axis, demonstrates the coexistence of diffraction spots associated with fcc-γ, γ-twin (γ_{tw}), and hcp-ε phase (Fig. 4g). The presence of continuous streaking on SADP (indicated in Fig. 4g) corresponds to high density {0001}/{111} SFs. Such ε-γ-γ_{tw} lamellar dual-phase structure is generated by the hcp → fcc shear transformation through the nucleation and propagation of Shockley partial dislocations. The corresponding deformation mechanisms will be discussed based on high-resolution TEM (HRTEM) characterizations.

3.3. Dynamically reversible shear transformation mechanisms at cryogenic temperature

The cryogenic temperature plastic deformation is dominated by the fcc → hcp shear transformation mechanism via successively gliding of Shockley partial dislocations, leading to the transformation from the initial fcc-phase grains to hcp-phase grains. Besides fcc → hcp shear transformation bands, plastic deformation in hcp-phase grains can also be accommodated by slips associated with

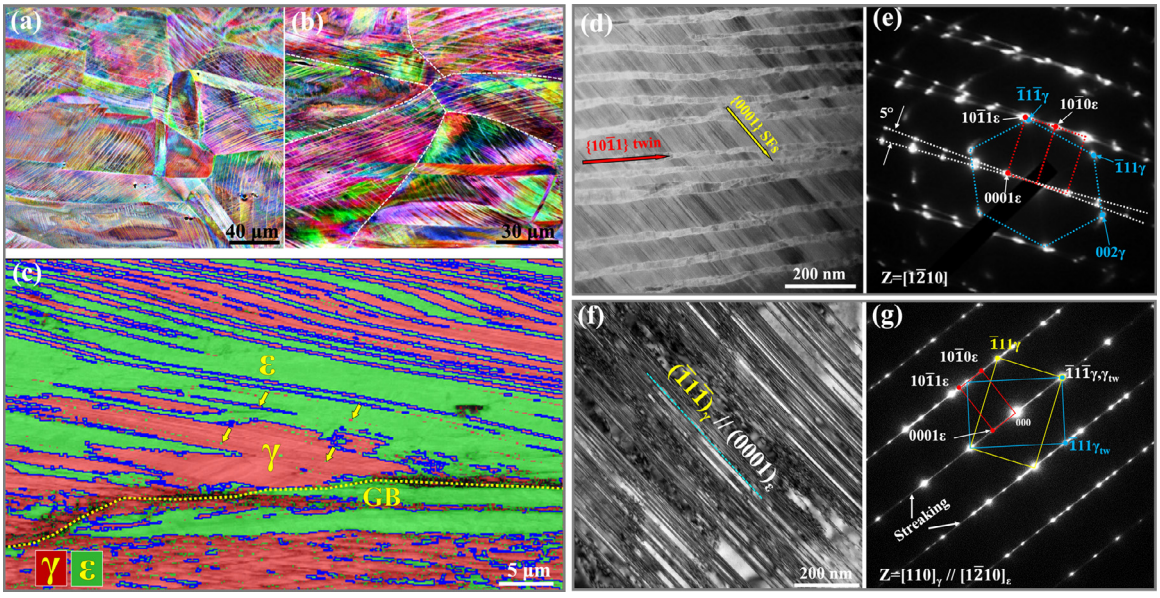

Fig. 4. Deformation-induced NL-DP structures. The COCI images of the deformed sample at 4.2 K up to a strain of (a) 20% and (b) 50%, showing numerous nano-spaced deformation bands within each grain. (c) EBSD phase map of the sample at a tension strain of 50%, showing lamellar dual-phase structure. (d) LAADF-STEM image showing the nano-laminated structures with numerous {10$\bar{1}$1} twins and high-density basal SFs, (e) corresponding indexed SADP. (f) The bright-field TEM image of the lamellar ε-γ-γ_{tw} dual-phase structures, (g) corresponding indexed SADP.

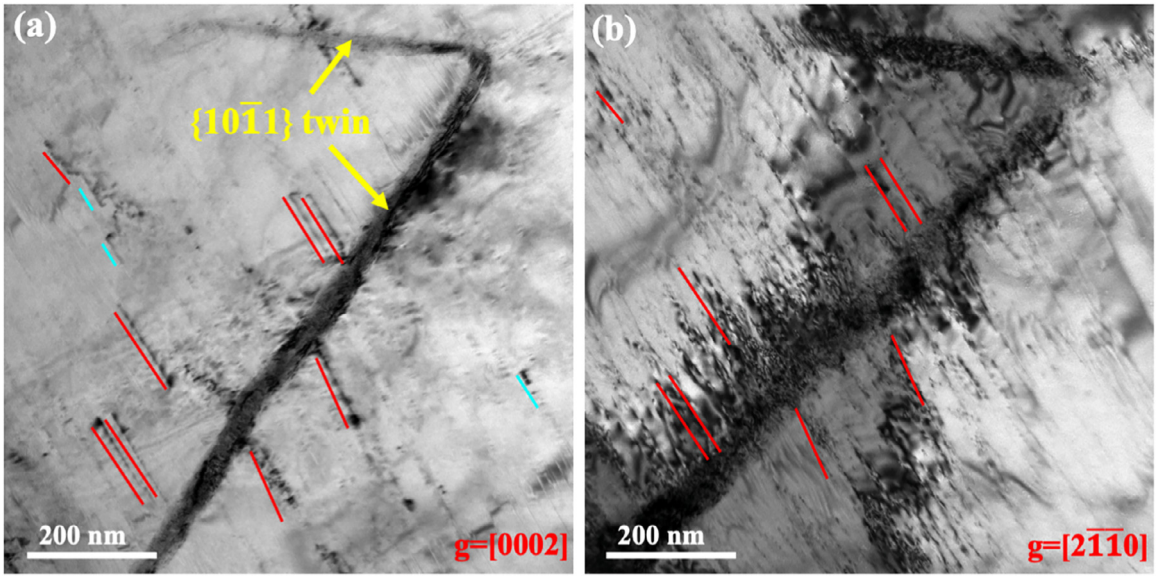

Fig. 5. Non-basal slip systems in hcp grains in the sample after tension to fracture at 4.2 K. TEM images obtained under various two-beam conditions, (a) at g=[0002], and (b) at g=[2$\bar{1}\bar{1}$0]. The dislocations marked by red lines are $\langle c+a \rangle$ dislocations. The dislocations marked by aqua lines are ⟨c⟩ dislocations.

gliding of ⟨a⟩, ⟨c⟩ and $\langle c+a \rangle$ dislocations. Fig. 5 shows two TEM images obtained under various two-beam conditions. Non-basal dislocations in hcp grains that are created by tensile deformation at 4.2 K are characterized with g=[0002] and g=[2$\bar{1}\bar{1}$0]. The dislocations marked by red lines are always visible under g=[0002] and g=[2$\bar{1}\bar{1}$0] two-beam conditions, suggesting that they are $\langle c+a \rangle$ dislocations. The dislocations marked by aqua lines are visible under the g=[0002] two-beam condition (Fig. 5a), but invisible under the g=[2$\bar{1}\bar{1}$0] two-beam condition (Fig. 5b), meaning that they are ⟨c⟩ dislocations. Other dislocations which are invisible under the g=[0002] two-beam condition and visible under the g=[2$\bar{1}\bar{1}$0] two-beam condition are ⟨a⟩ dislocations. However, these deformation mechanisms cannot account for the thermomechanical instability, i.e., serrated flow behavior at 4.2 K.

Considering the cryogenic temperature deformation condition and the formation of two types of shear transformation bands, we speculated that the deformation-induced dissipative heating can lead to adiabatic heating locally at cryogenic temperature, stimulating localized avalanche shear and the localized thermal softening (thermomechanical instability) [37,38]. Correspondingly, we observed the periodical load drop. Such thermal softening demands a very small difference in the Gibbs free energy between fcc-γ and hcp-ε phases of $Cr_{26}Mn_{20}Fe_{20}Co_{20}Ni_{14}$ HEA [29]. According to the previous calculations of adiabatic heating in CrMnFeCoNi HEA systems [20,39], the local dissipative heating during straining can reach up to ∼ 153 K at 4.2 K. Such high local temperature fluctuation is sufficient to facilitate the dynamical and alternate occurrence of fcc → hcp and hcp → fcc shear transforma-

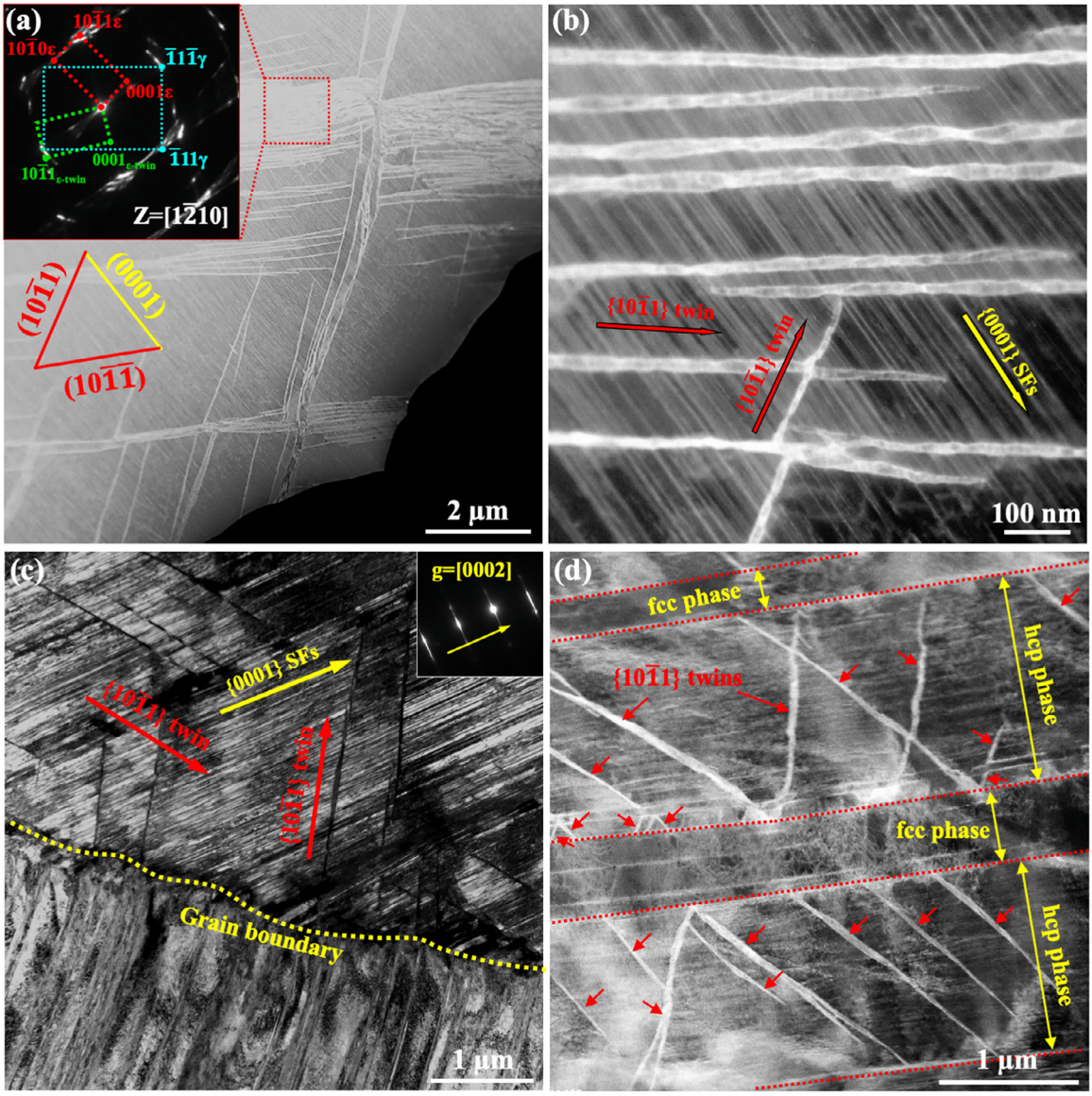

Fig. 6. High-density {10$\bar{1}$1} nano-twins and basal SFs. (a) Low-magnification with SADP inset and (b) high-magnification LAADF-STEM images, showing high-density {10$\bar{1}$1} twins and basal SFs. (c) TEM image of {10$\bar{1}$1} twins at grain boundaries, obtained with two-beam condition g=[0002]. (d) LAADF-STEM image showing two {10$\bar{1}$1} twin variants at the fcc-hcp phase boundaries.

tions during deformation at 4.2 K, leading to lamellar dual-phase structures.

For an hcp grain, plastic deformation is accommodated by dislocations and twins, and even by adiabatic heating stimulated reverse phase transformation. Here, we performed TEM observations of the two types of nano-laminated dual-phase bands and rationalized the corresponding shear transformation mechanisms. Mechanism #1 is described by $\gamma \rightarrow \varepsilon \rightarrow$ {10$\bar{1}$1} twin $\rightarrow \gamma/\gamma_{tw}$. The LAADF-STEM images in Fig. 6a, b, with the SADP inset, show ultrahigh-density of {0001} SFs, {10$\bar{1}$1} twin variants, and {111} fcc bands in hcp grains, leading to three sets of parallel bands. {0001} SFs and {111} fcc bands are parallel to each other. Such shears on basal planes do not contribute to plastic deformation in the ⟨c⟩ axis. Therefore, {10$\bar{1}$1} twinning was activated to accommodate shear on non-basal planes, leading to the formation of numerous {10$\bar{1}$1} nano-twins in the hcp-ε phase. It is observed that {10$\bar{1}$1} twins are connected to grain boundaries (Fig. 6c) or the fcc-hcp phase boundaries (Fig. 6d), suggesting that they are nucleated at and/or blocked by grain/phase boundaries.

The substructures of {10$\bar{1}$1} twins were further characterized by HRTEM. Fig. 7a shows the twin tip, {10$\bar{1}$1} coherent twin boundaries, and pyramidal/basal steps/facets at twin boundaries. The misorientation angle of basal planes between the twin and matrix is about 123.0°, which is close to the theoretical misorientation angle (123.8°) of {10$\bar{1}$1} twin. Fig. 7b is a high-resolution LAADF-STEM image taken from a {10$\bar{1}$1} twin boundary, showing that the {10$\bar{1}$1} twin has been partially transformed into fcc structure and the coherent twin boundary containing steps. It is noted that the part of the {10$\bar{1}$1} twin displays an fcc structure marked by γ in Fig. 7a–d. As shown in Fig. 7a, the typical Shoji-Nishiyama orientation relationship between fcc and hcp structure inside the {10$\bar{1}$1} twin, i.e., $[110]_\gamma$ // $[1\bar{2}10]_\varepsilon$ and $(\bar{1}1\bar{1})_\gamma$ // $(0001)_\varepsilon$, suggests that the hcp $\rightarrow$ fcc shear transformation ($\varepsilon \rightarrow \gamma$) is accomplished through gliding of Shockley partial dislocations on every other basal plane. When the {10$\bar{1}$1} twins transform into fcc structure, Shockley partial dislocations are activated on {111} planes, leading to formation of {111} SFs and {111} nano-twins in the newly formed fcc domain, as shown in Fig. 7c. Fig. 7d shows

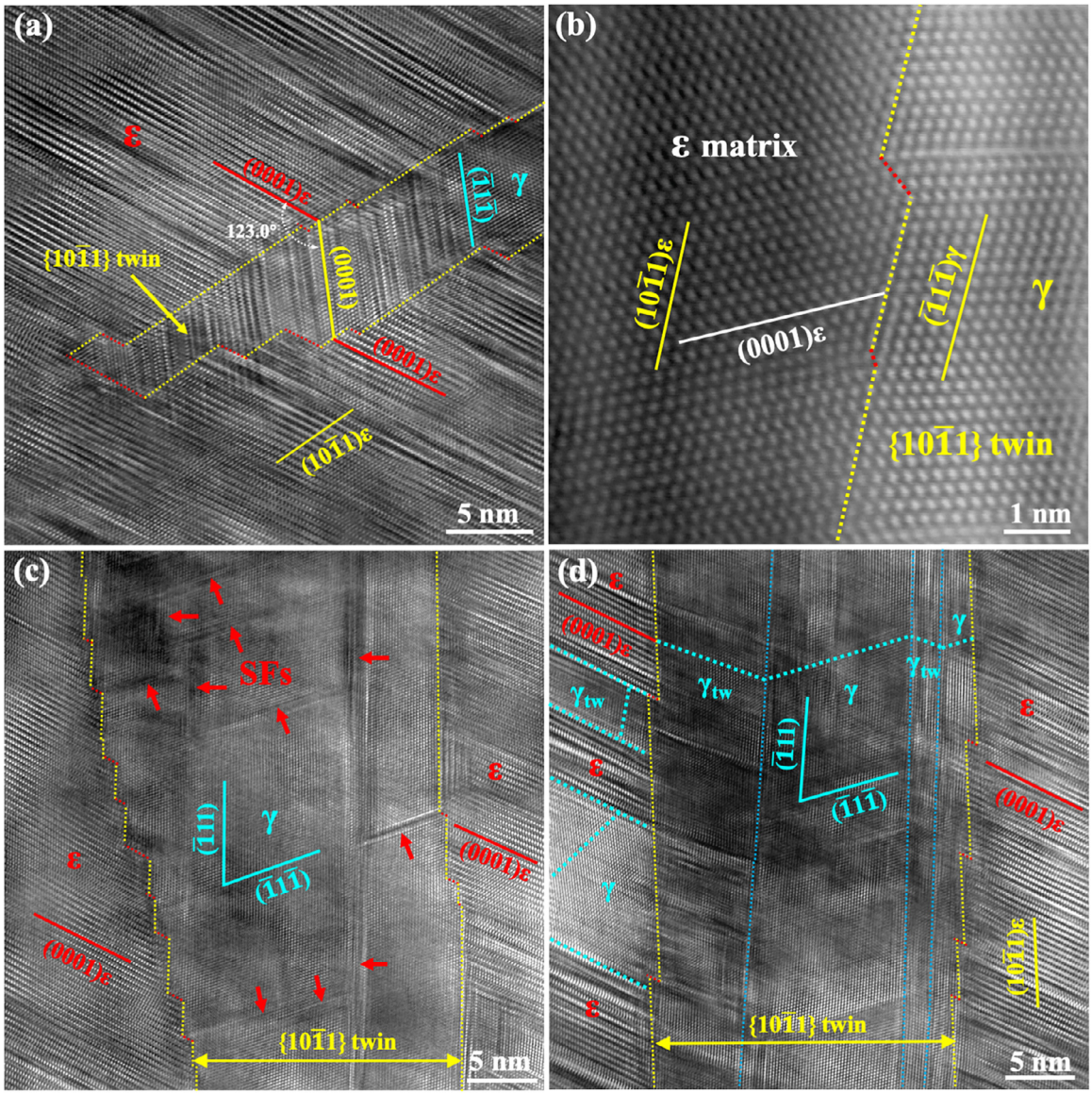

Fig. 7. (a) HRTEM image of a {10$\bar{1}$1} twin tip taken along the [1$\bar{2}$10]$_\varepsilon$ zone axis, showing fcc domain in the twin. (b) Atomic-scale interface structure of the hcp-ε matrix and {10$\bar{1}$1} twins. (c) HRTEM image showing that a {10$\bar{1}$1} twin transforms to fcc structure with {111} SFs. (d) HRTEM image showing that a {10$\bar{1}$1} twin transforms into two fcc domains with the twin orientation.

two fcc domains with {111} twin orientation inside an {10$\bar{1}$1} twin. In addition, the hcp-ε matrix surrounding the {10$\bar{1}$1} twin also experience reverse hcp → fcc shear transformation, leading to formation of nanoscale γ/γ_{tw} bands (Fig. 7d). Correspondingly, we proposed a multiple-step shear transformation mechanism, i.e., $\gamma \rightarrow \varepsilon \rightarrow$ {10$\bar{1}$1} twin → γ/γ_{tw}. The $\gamma \rightarrow \varepsilon$ shear transformation is promoted by low SFE at cryogenic temperature. The $\varepsilon \rightarrow$ {10$\bar{1}$1} twinning accommodates plastic strain along the ⟨c⟩ in hcp grains, while the local dissipative heating stimulates the {10$\bar{1}$1} twin → γ reverse shear transformation, causing mechanical softening (stress drop) and developing a new orientation relationship between hcp and fcc structure, i.e., $[110]_\gamma$ // $[1\bar{2}10]_\varepsilon$ and $(\bar{1}1\bar{1})_\gamma$ // $(10\bar{1}1)_\varepsilon$, as evidenced in Fig. 7b.

Corresponding to the typical fcc/hcp nano-laminated structure shown in Fig. 8a, the shear transformation mechanism #2 is described by $\gamma \rightarrow \varepsilon \rightarrow \gamma/\gamma_{tw}$. For high-density of basal SFs in the hcp-ε phase, the faulted regions can transform back into fcc structure through correcting SFs via nucleation and glide of Shockley partial dislocations, which is energetically favorable since the process will reduce the density of SFs. It is noted that fcc laminates frequently have two orientations, forming a {111} twin orientation relationship (Fig. 8a). Corresponding to the Shoji-Nishiyama orientation relationship, the hcp → fcc phase transformation is accomplished via gliding of Shockley partial dislocations on every two {0001} planes. As shown in Fig. 8b, the front of the phase boundary is very sharp and perpendicular to the {111}||{0001} habit planes, suggesting that these dislocations attract each other [40]. Therefore, this sharp interface should be described by a group of Shockley partial dislocations with Burgers vectors b_1, b_2, and b_3 in a repeatable unit [41,42], …b_2:b_1:b_3…, as schematically illustrated in Fig. 8c. Note that the Shockley partial dislocations in an unit have a net zero Burgers vector (Fig. 8d). Based on HRTEM observations (Fig. 8b), six-layer phase boundary and eighteen-layer phase boundary are identified, corresponding to one unit and three units, as schematically illustrated in Fig. 8c. The hcp structure transforms into an fcc structure through gliding of sharp steps with three

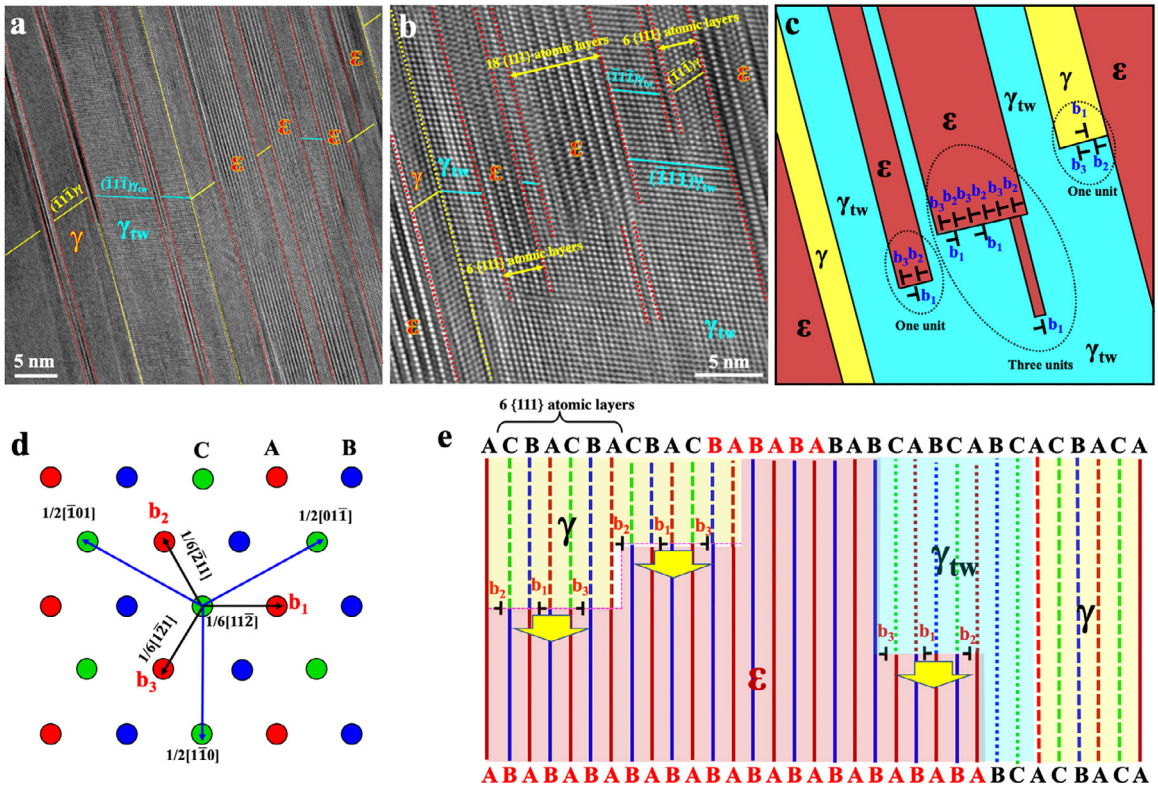

Fig. 8. Shear transformation of $\gamma \rightarrow \varepsilon \rightarrow \gamma/\gamma_{tw}$. (a) HRTEM image of the HEA after tension to a strain of 50% at 4.2 K, showing the typical ε-γ-γ_{tw} NL-DP structure. (b) HRTEM image showing several sharp interfaces with six and eighteen close-packed atomic planes. (c) Corresponding schematic illustration of the sharp phase boundaries that can be described by an array of Shockley partial dislocations (…b_2:b_1:b_3…). (d) Three Burgers vectors of Shockley partial dislocations. (e) Schematic illustration of the $\varepsilon \rightarrow \gamma/\gamma_{tw}$ shear transformation mechanism through gliding of a group of Shockley partial dislocations.

Shockley partial dislocations as one unit. Fig. 8e schematically illustrates the $\varepsilon \rightarrow \gamma$ and $\varepsilon \rightarrow \gamma_{tw}$ transformation mechanisms through collective gliding of three Shockley partial dislocations on every two basal planes (corresponds to six atomic planes in a unit). Note that the collective gliding mechanism of three Shockley partial dislocations does not need any applied shear stress [40,43]. The driving force for the reverse hcp → fcc phase transformation is ascribed to the decrease in cohesive energy because the fcc structure has lower cohesive energy than the hcp structure due to deformation-induced local dissipative heating. Thus, this new shear transformation mechanism ($\gamma \rightarrow \varepsilon \rightarrow \gamma/\gamma_{tw}$) requires the assistance of temperature fluctuations caused by plastic deformation at 4.2 K to overcome the energy barrier of martensitic phase transformation between hcp-ε and fcc-γ phases. The path of $\gamma \rightarrow \varepsilon \rightarrow \gamma/\gamma_{tw}$ can well explain the concurrence of deformation-induced reverse shear transformation, and the corresponding formation of hcp-twin lamellae substructures in fcc HEAs with low SFE after deformation at ultralow temperatures [12,19,36,44-48].

3.4. Application of cryogenic temperature promoted NL-DP structures

Corresponding to the two shear transformation mechanisms, fcc-phase $Cr_{26}Mn_{20}Fe_{20}Co_{20}Ni_{14}$ HEA develops dynamic NL-DP structures at cryogenic temperature, more importantly, the volume ratio and their thicknesses of the two phases dynamically increase and decrease accompanied by mechanical loading and heating stimulated softening. The exceptional strength-ductility-strain hardening ability combination at 4.2 K is thus attributed to the synergistic effects of the two shear transformation mechanisms, which generate steady strain-hardening sources of coherent interfaces. More importantly, the dynamic evolution of two phases relaxes the local stress concentrations associated with dislocation accumulations along interfaces, preventing crack initiation and improving ductility.

To demonstrate the strength-ductility effects associated with the NL-DP structures, we tailored the microstructure of the fcc-phase $Cr_{26}Mn_{20}Fe_{20}Co_{20}Ni_{14}$ HEA by stretching up to a strain of 20% at 4.2 K and then tempering it at 773 K (less than recrystallization temperature) for 1 h. In comparison, we also stretched the alloy up to a strain of 20% at 298 K, and then tempered the deformed sample at 773 K for 1 h. As shown in Fig. 9a, b, the pre-straining at 298 K leads to an increase in yield strength but reduces the ductility and strain-hardening capability. However, the pre-straining at 4.2 K significantly improves the yield strength and tensile strength without loss of strain-hardening capability and ductility (Fig. 9a, b). The yield strength is about 525 MPa, two times stronger than that of the annealed counterparts without pre-straining (252 MPa). The uniform elongation is ~55%, the same as the annealed counterparts. The failure characteristics of the pre-strained sample at 4.2 K display typical ductile dimpled structures without macroscopic necking (Fig. 9c, d), which differs from other ductile fcc HEAs whose fracture is induced by necking at room temperature. The different mechanical properties between the pre-strained samples at 298 K and 4.2 K are attributed to their microstructures. The pre-strained sample at 298 K contains high-density dislocations since plastic deformation is mainly accommodated by dislocation slip [49], while the pre-strained sample at 4.2 K develops NL-DP structures with high-density interfaces such as γ-twin boundaries, γ-ε phase boundaries, and {10$\bar{1}$1} twin boundaries.

When the pre-strained HEA at 4.2 K is deformed at room temperature, the hcp phase formed during pre-straining plasti-

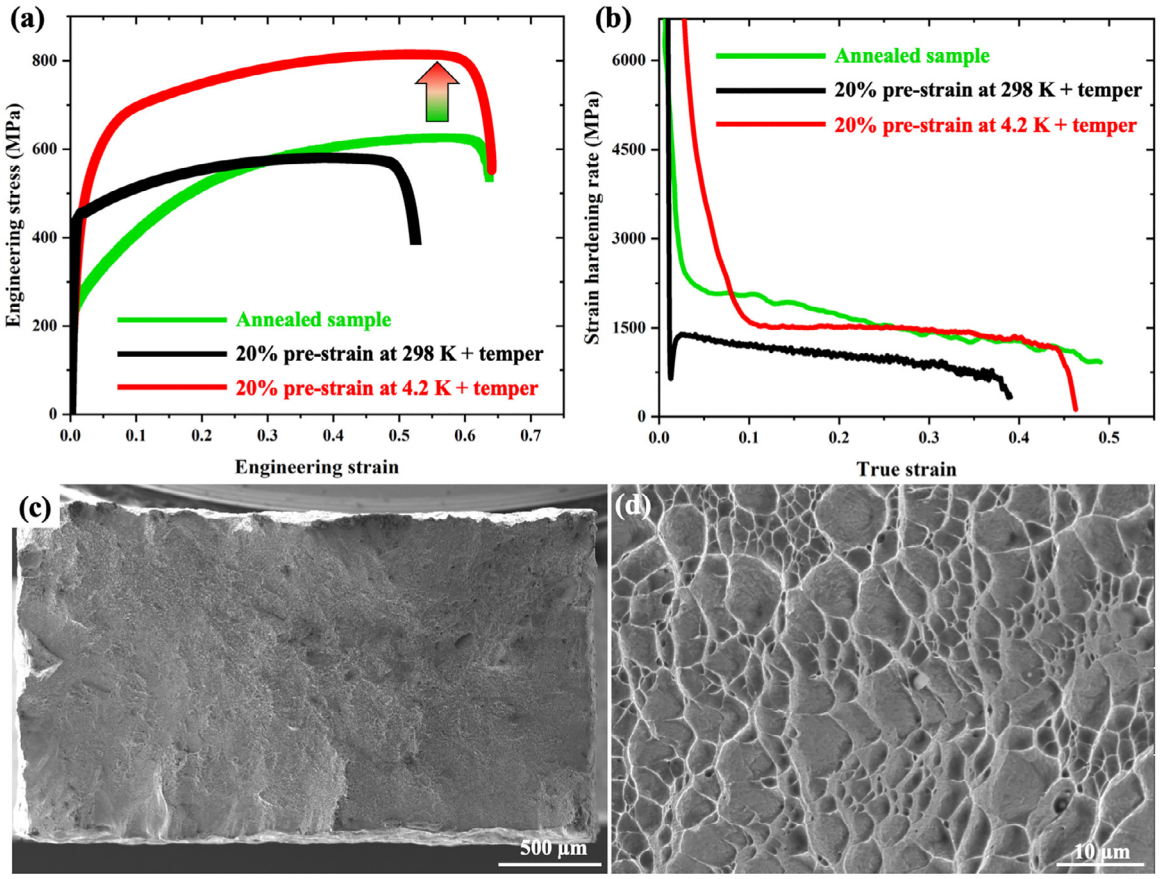

Fig. 9. Room-temperature mechanical properties of the pre-strained samples. (a) The room-temperature tensile stress-strain curves of the 20% pre-strained (at 4.2 K and 298 K) and tempered samples, together with the annealed sample for comparison. (b) The corresponding strain-hardening curves of the annealed and pre-strained samples. The pre-straining at 4.2 K shows a great potential to evade the strength-ductility dilemma. (c, d) Tensile fracture characteristics showing the ductile dimpled structures of the sample after pre-straining at 4.2 K, without necking.

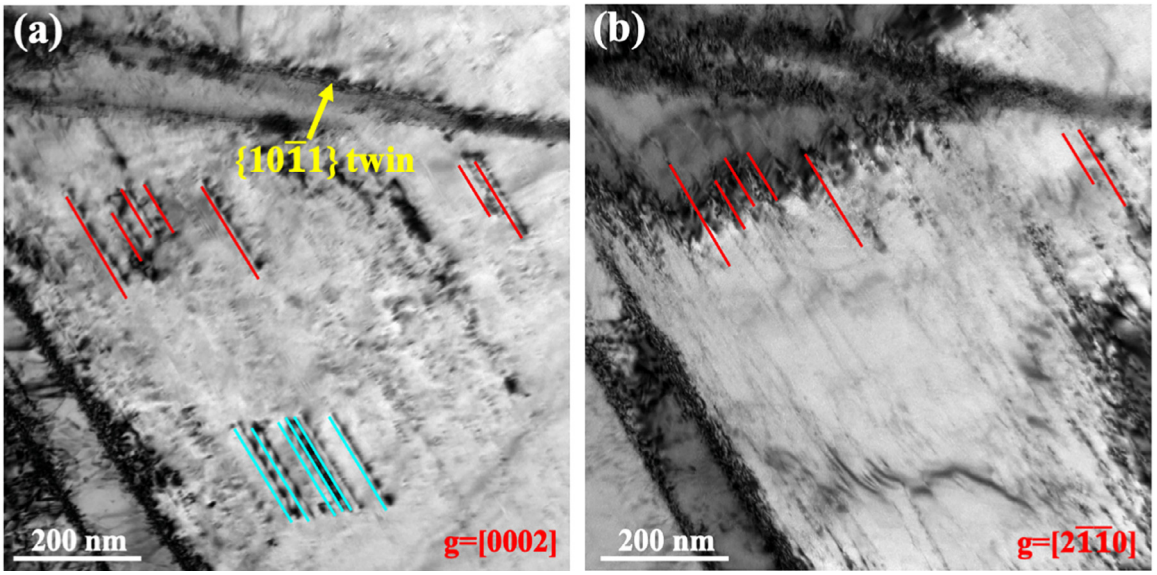

Fig. 10. Non-basal slip systems in hcp grains in the pre-strained sample after tension to fracture at room temperature. TEM images obtained under various two-beam conditions, (a) at g=[0002], and (b) at g=[2$\bar{1}\bar{1}$0]. The dislocations marked by red lines are $\langle c + a \rangle$ dislocations. The dislocations marked by aqua lines are $\langle c \rangle$ dislocations.

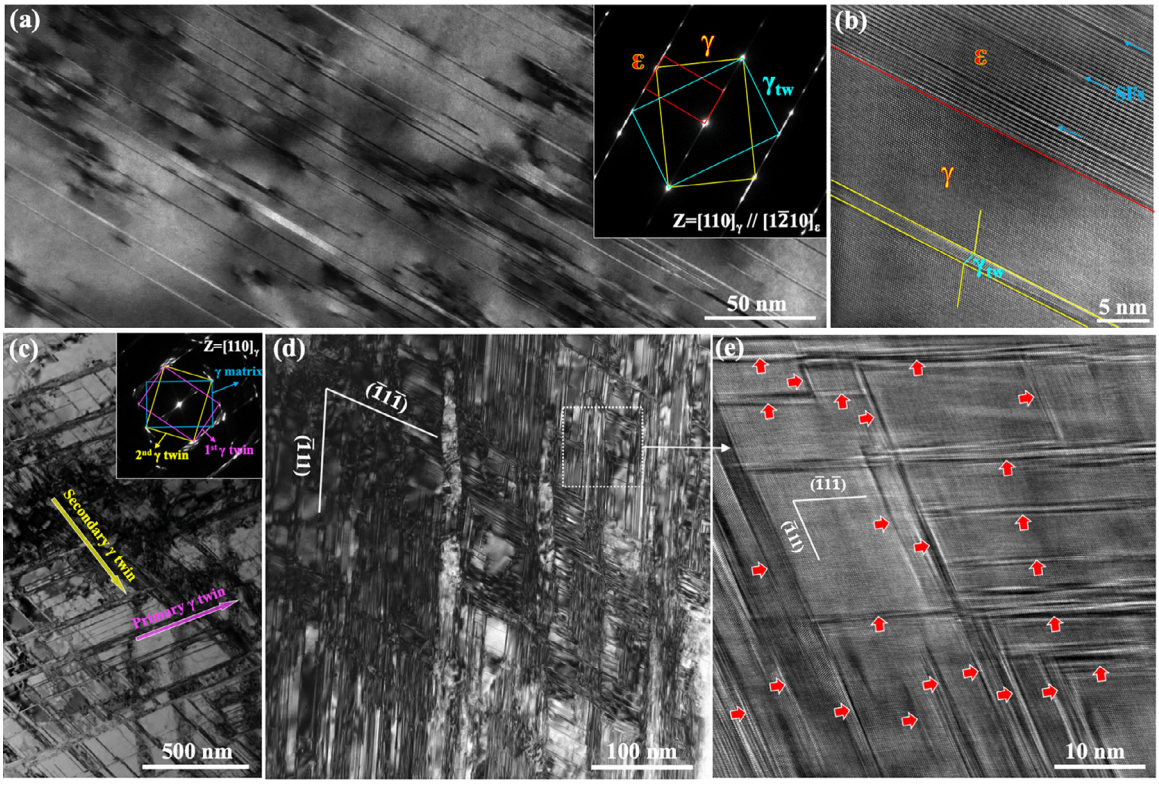

Fig. 11. Strengthening mechanism of the ε-γ-γ_{tw} NL-DP structure. (a) Bright-field TEM image with SADP inset, and (b) corresponding HRTEM image showing the reverse phase transformation from the hcp-ε to fcc γ/γ_{tw} phases. (c) Low-magnification and (d) high-magnification of bright-field TEM images, with SADP inset, and (e) HRTEM image of the 20% pre-strained (pre-strained at 4.2 K) sample after tension to fracture at room temperature, showing numerous SFs within ε-γ-γ_{tw} NL-DP structure.

cally deform via dislocations and reverse phase transformation. Fig. 10 shows dislocation activities in the hcp phase in the sample after tension to fracture. Based on the TEM characterizations under two-beam conditions (g=[0002] and g=[2$\bar{1}\bar{1}$0]), ⟨a⟩, ⟨c⟩, and ⟨$c + a$⟩ dislocations are observed, indicating the occurrence of both basal slips and non-basal slips in hcp phase at room temperature. This is in a good agreement with the previously reported ductile high-entropy hcp phase in FeMnCoCr HEA [50].

Once reverse phase transformation happens locally, Shockley partial or full dislocations on {111} planes non-parallel to the laminates will interact with the pre-formed interfaces associated with the laminated dual-phase structure, and dislocations will pile up along the interfaces. As shown in Fig. 11a, b, the hcp phase in the sample after tension to fracture partly transform to γ/γ_{tw} via motions of Shockley partial dislocations on basal planes. Due to the low SFE and fine-scale laminates, Shockley partial dislocations will dominate plastic deformation, generating a high density of SFs or nanotwins in pre-formed laminates. The typical bright-field TEM image of the 20%-strained sample (pre-strained at 4.2 K) show high-density γ primary nanotwins and secondary nanotwins, and their intersections, but less hcp phase after tension to fracture at room temperature, as shown in Fig. 11c with SADP inset. The TEM (Fig. 11d) and corresponding HRTEM (Fig. 11e) images show the formation of ultrahigh-density {111} SFs and their interactions between the twin boundaries. Therefore, reverse phase transformation (hcp → fcc), twin-twin interactions, SF-SF interactions, and activities between twin boundaries and partial dislocations contribute greatly to the enhanced strength, strain-hardening ability, and ductility.

When {10$\bar{1}$1} twins are pre-induced in hcp grains, the hcp phase exhibits high stability during deformation at room temperature. Fig. 12a, b are the typical dark-field TEM images of the pre-strained coherent nano-lamellar sample after tension to fracture at 298 K, highlighted respectively by the $\{0001\}_{\varepsilon}$ and $\{111\}_{\gamma}$ diffraction spots as indicated in corresponding SADP in Fig. 12c. We note that the regions between {10$\bar{1}$1} nanotwins retain hcp structure in the pre-strained sample after tension to fracture at room temperature (Fig. 12a). The dark-field TEM image in Fig. 12b and corresponding SADP in Fig. 12c demonstrates that most of the {10$\bar{1}$1} twins have been transformed into fcc-γ and γ-twins, which provides numerous deformation channels to promote the plastic deformation in hcp-ε matrix during mechanical loading at 298 K. As shown in Fig. 12d, the typical LAADF-STEM image of the nano-laminated hcp-ε phase shows a high-density of nanoscale {10$\bar{1}$1} twins. Plastic deformation in {10$\bar{1}$1} nanotwins is accommodated by Shockley partial dislocations on close-packed planes and hcp → fcc shear transformation mechanisms, as evidenced in Fig. 12e, f. The high-resolution LAADF-STEM image in Fig. 12e shows that the ultrahigh-density of γ-nanotwins and SFs subdivide the ~15 nm-wide {10$\bar{1}$1} twin into a sub-1 nm-thick twin/SFs/matrix lamellar nanostructure. Fig. 12f is a high-resolution LAADF-STEM image of the {10$\bar{1}$1} twin boundary, where the surrounding ε-matrix and {10$\bar{1}$1} twin has been partly transformed into fcc structure with the orientation relationship of $[110]_{matrix}$ // $[110]_{twin}$ and $(\bar{1}11)_{matrix}$ // $(002)_{twin}$. Note that the {10$\bar{1}$1} twin exhibits much higher density of SFs and nanotwins than that in the hcp matrix (Fig. 12d, e), indicating pronounced motions of Shockley dislocations within {10$\bar{1}$1} twin, nucleated from the {10$\bar{1}$1} twin boundaries. It should be noted that the {10$\bar{1}$1} twin-matrix interface (indicated in Fig. 12f) is an unconventional 'twin plane' since the matrix and twin have been transformed into the fcc structure. This special interface can have an important strengthening effect by impeding the motion of dislocations.

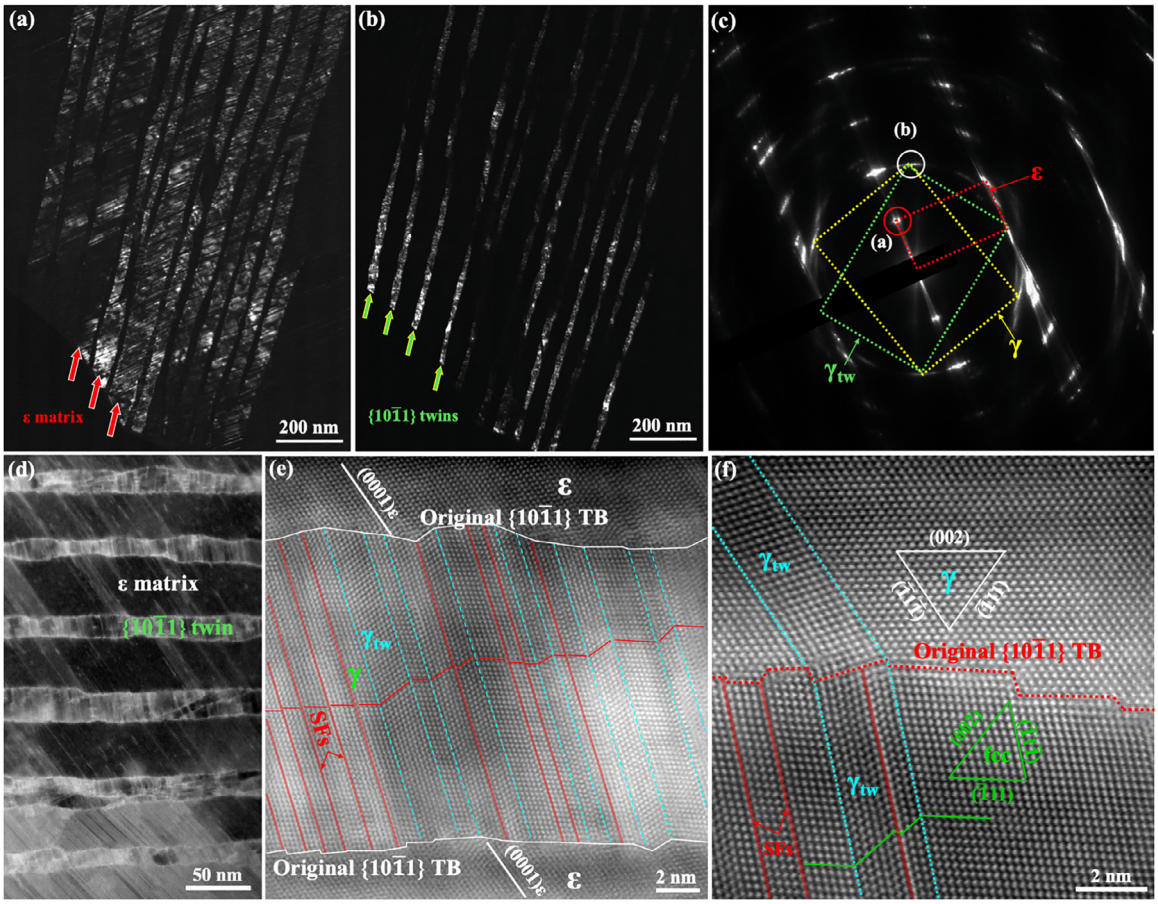

Fig. 12. Strengthening mechanism of the {10$\bar{1}$1} twin boundaries. (a), (b) Dark-field TEM images of the 20% pre-strained sample after tension to fracture at room temperature highlighted by ε and γ/γ_{tw} superlattice spots, respectively. (c) Corresponding SADP showing three sets of diffraction spots from ε, γ, and γ_{tw}. (d) Low-magnification and (e) high-resolution LAADF-STEM images of the {10$\bar{1}$1} twins, showing the ~1 nm-thick γ/γ_{tw}/SFs nano-laminated structure within {10$\bar{1}$1} twin. (f) High-resolution LAADF-STEM image showing that a {10$\bar{1}$1} twin transforms into fcc structure and the hcp matrix also transforms into fcc structure, and {111} nanotwins form in and out of the {10$\bar{1}$1} twin.

4. Conclusion

We revealed two anomalous shear transformation mechanisms at cryogenic temperature, featured by $\gamma \rightarrow \varepsilon \rightarrow$ {10$\bar{1}$1} twin $\rightarrow \gamma/\gamma_{tw}$ and $\gamma \rightarrow \varepsilon \rightarrow \gamma/\gamma_{tw}$, which dynamically generate nano-laminated dual-phase structures in a single-phase fcc $Cr_{26}Mn_{20}Fe_{20}Co_{20}Ni_{14}$ HEA and advance the "dynamic Hall-Petch" effect in improving strength, ductility, and strain-hardening capability. The $\gamma \rightarrow \varepsilon$ shear transformation is promoted by low SFE at cryogenic temperature. The $\varepsilon \rightarrow \gamma$ reverse shear transformation is stimulated by the local dissipative heating. The small difference in cohesive energy between γ and ε phases at low temperatures enables the dynamically reversible shear transformation. {10$\bar{1}$1} twinning accommodates plastic strain along the ⟨c⟩ in hcp grains, while the local dissipative heating associated with {10$\bar{1}$1} twinning promotes the reverse shear transformation. Our work demonstrates that tailoring SFE and optimizing deformation temperature could promote both shear transformation and corresponding reverse shear transformation in metastable alloys and dynamically develop laminated dual-phase structures which can simultaneously enhance the strength, strain-hardening capability, and ductility.

Declaration of competing interest

The authors declare no competing financial interests

Acknowledgments

The authors acknowledge the financial support from the National Natural Science Foundation of China (No. 52002109, 51771201, 52071124), the Natural Science Foundation of the Hebei province (No. E2020202088, E2021202135), the key project of the Natural Science Foundation of Tianjin (No. 20JCZDJC00440), the Overseas Scientists Sponsorship Program by Hebei Province (C20210331), and Open Research Fund from the State Key Laboratory of Rolling and Automation, Northeastern University [Grant No. 2020RALKFKT002].

References

[1] R.O. Ritchie, The conflicts between strength and toughness, Nat. Mater. 10 (11) (2011) 817–822.
[2] M.E. Launey, R.O. Ritchie, On the fracture toughness of advanced materials, Adv. Mater. 21 (20) (2009) 2103–2110.
[3] S.Z. Han, E.A. Choi, S.H. Lim, S. Kim, J. Lee, Alloy design strategies to increase strength and its trade-offs together, Prog. Mater. Sci. 117 (2020).
[4] H. Wu, G. Fan, An overview of tailoring strain delocalization for strength-ductility synergy, Prog. Mater. Sci. 113 (2020) 100675.
[5] B.C. De Cooman, Y. Estrin, S.K. Kim, Twinning-induced plasticity (TWIP) steels, Acta Mater 142 (2018) 283–362.
[6] M.M. Wang, C.C. Tasan, D. Ponge, A.C. Dippel, D. Raabe, Nanolaminate transformation-induced plasticity-twinning-induced plasticity steel with dynamic strain partitioning and enhanced damage resistance, Acta Mater 85 (2015) 216–228.
[7] M. Soleimani, A. Kalhor, H. Mirzadeh, Transformation-induced plasticity (TRIP) in advanced steels: a review, Mater. Sci. Eng. A (2020) 140023.

[8] J. Su, D. Raabe, Z. Li, Hierarchical microstructure design to tune the mechanical behavior of an interstitial TRIP-TWIP high-entropy alloy, Acta Mater 163 (2019) 40–54.
[9] H. Beladi, I. Timokhina, Y. Estrin, J. Kim, B. De Cooman, S. Kim, Orientation dependence of twinning and strain hardening behaviour of a high manganese twinning induced plasticity steel with polycrystalline structure, Acta Mater 59 (20) (2011) 7787–7799.
[10] I. Gutierrez-Urrutia, D. Raabe, Dislocation and twin substructure evolution during strain hardening of an Fe-22wt.% Mn-0.6wt.% C TWIP steel observed by electron channeling contrast imaging, Acta Mater 59 (16) (2011) 6449–6462.
[11] I. Karaman, H. Sehitoglu, A. Beaudoin, Y.I. Chumlyakov, H. Maier, C. Tome, Modeling the deformation behavior of Hadfield steel single and polycrystals due to twinning and slip, Acta Mater 48 (9) (2000) 2031–2047.
[12] Z. Li, K.G. Pradeep, Y. Deng, D. Raabe, C.C. Tasan, Metastable high-entropy dual-phase alloys overcome the strength-ductility trade-off, Nature 534 (7606) (2016) 227–230.
[13] E. Ma, X. Wu, Tailoring heterogeneities in high-entropy alloys to promote strength-ductility synergy, Nat. Commun. 10 (1) (2019) 1–10.
[14] B. Cantor, Multicomponent high-entropy Cantor alloys, Prog. Mater. Sci. 120 (2020) 100754.
[15] E.P. George, W.A. Curtin, C.C. Tasan, High entropy alloys: a focused review of mechanical properties and deformation mechanisms, Acta Mater 188 (2020) 435–474.
[16] Z. Li, S. Zhao, R.O. Ritchie, M.A. Meyers, Mechanical properties of high-entropy alloys with emphasis on face-centered cubic alloys, Prog. Mater. Sci. 102 (2019) 296–345.
[17] P. Sathiyamoorthi, H.S. Kim, High–entropy alloys with heterogeneous microstructure: processing and mechanical properties, Prog. Mater. Sci. (2020) 100709.
[18] A.H.B. Gludovatz, D. Catoor, E.H. Chang, E.P. George, R.O. Ritchie, A fracture-resistant high-entropy alloy for cryogenic applications, Science 345 (2014) 1153–1158.
[19] S. Chen, H.S. Oh, B. Gludovatz, S.J. Kim, E.S. Park, Z. Zhang, R.O. Ritchie, Q. Yu, Real-time observations of TRIP-induced ultrahigh strain hardening in a dual-phase CrMnFeCoNi high-entropy alloy, Nat. Commun. 11 (1) (2020) 1–8.
[20] W. Lu, C.H. Liebscher, G. Dehm, D. Raabe, Z. Li, Bidirectional transformation enables hierarchical nanolaminate dual-phase high-entropy alloys, Adv. Mater. 30 (44) (2018) e1804727.
[21] M. Naeem, H. He, F. Zhang, H. Huang, S. Harjo, T. Kawasaki, B. Wang, S. Lan, Z. Wu, F. Wang, Cooperative deformation in high-entropy alloys at ultralow temperatures, Sci. Adv. 6 (13) (2020) eaax4002.
[22] Z. Zhang, M.M. Mao, J. Wang, B. Gludovatz, Z. Zhang, S.X. Mao, E.P. George, Q. Yu, R.O. Ritchie, Nanoscale origins of the damage tolerance of the high–entropy alloy CrMnFeCoNi, Nat. Commun. 6 (2015) 10143.
[23] Z. Zhang, H. Sheng, Z. Wang, B. Gludovatz, Z. Zhang, E.P. George, Q. Yu, S.X. Mao, R.O. Ritchie, Dislocation mechanisms and 3D twin architectures generate exceptional strength-ductility-toughness combination in CrCoNi medium-entropy alloy, Nat. Commun. 8 (2017) 14390.
[24] F. Otto, A. Dlouhý, C. Somsen, H. Bei, G. Eggeler, E.P. George, The influences of temperature and microstructure on the tensile properties of a CoCrFeMnNi high-entropy alloy, Acta Mater 61 (15) (2013) 5743–5755.
[25] J. Su, X. Wu, D. Raabe, Z. Li, Deformation-driven bidirectional transformation promotes bulk nanostructure formation in a metastable interstitial high entropy alloy, Acta Mater 167 (2019) 23–39.
[26] S. Huang, W. Li, S. Lu, F. Tian, J. Shen, E. Holmström, L. Vitos, Temperature dependent stacking fault energy of FeCrCoNiMn high entropy alloy, Scr. Mater. 108 (2015) 44–47.
[27] S. Huang, H. Huang, W. Li, D. Kim, S. Lu, X. Li, E. Holmström, S.K. Kwon, L. Vitos, Twinning in metastable high-entropy alloys, Nat. Commun. 9 (1) (2018) 1–7.
[28] M. Jo, Y.M. Koo, B.J. Lee, B. Johansson, L. Vitos, S.K. Kwon, Theory for plasticity of face-centered cubic metals, Proc. Natl. Acad. Sci. 111 (18) (2014) 6560–6565.
[29] S. Zhao, G.M. Stocks, Y. Zhang, Stacking fault energies of face-centered cubic concentrated solid solution alloys, Acta Mater 134 (2017) 334–345.
[30] K. Ming, W. Lu, Z. Li, X. Bi, J. Wang, Amorphous bands induced by low temperature tension in a non-equiatomic CrMnFeCoNi alloy, Acta Mater 188 (2020) 354–365.
[31] H. Zhao, M. Song, S. Ni, S. Shao, J. Wang, X. Liao, Atomic-scale understanding of stress-induced phase transformation in cold-rolled Hf, Acta Mater 131 (2017) 271–279.
[32] P.M. Anderson, J.P. Hirth, J. Lothe, Theory of Dislocations, Cambridge University Press, 2017.
[33] G. Laplanche, A. Kostka, C. Reinhart, J. Hunfeld, G. Eggeler, E.P. George, Reasons for the superior mechanical properties of medium-entropy CrCoNi compared to high-entropy CrMnFeCoNi, Acta Mater 128 (2017) 292–303.
[34] B. Gludovatz, A. Hohenwarter, K.V. Thurston, H. Bei, Z. Wu, E.P. George, R.O. Ritchie, Exceptional damage-tolerance of a medium-entropy alloy CrCoNi at cryogenic temperatures, Nat. Commun. 7 (2016) 10602.
[35] M. Shih, J. Miao, M. Mills, M. Ghazisaeidi, Stacking fault energy in concentrated alloys, Nat. Commun. 12 (1) (2021) 3590.
[36] H. He, M. Naeem, F. Zhang, Y. Zhao, S. Harjo, T. Kawasaki, B. Wang, X. Wu, S. Lan, Z. Wu, W. Yin, Y. Wu, Z. Lu, J.J. Kai, C.T. Liu, X.L. Wang, Stacking fault driven phase transformation in CrCoNi medium entropy alloy, Nano Lett 21 (2021) 1419–1426.
[37] V. Pustovalov, Serrated deformation of metals and alloys at low temperatures, Low Temp. Phys. 34 (9) (2008) 683–723.
[38] Z.S. Basinski, The instability of plastic flow of metals at very low temperatures, Proc. R. Soc. A 240 (1221) (1957) 229–242.
[39] G.C. Soares, M. Patnamsetty, P. Peura, M. Hokka, Effects of adiabatic heating and strain rate on the dynamic response of a CoCrFeMnNi High-Entropy Alloy, J. Dyn. Behav. 5 (3) (2019) 320–330.
[40] H. Zheng, J. Wang, J.Y. Huang, J. Wang, Z. Zhang, S.X. Mao, Dynamic process of phase transition from wurtzite to zinc blende structure in InAs nanowires, Nano Lett 13 (12) (2013) 6023–6027.
[41] J. Wang, O. Anderoglu, J. Hirth, A. Misra, X. Zhang, Dislocation structures of $\Sigma 3\{112\}$ twin boundaries in face centered cubic metals, Appl. Phys. Lett. 95 (2) (2009) 021908.
[42] J. Wang, N. Li, O. Anderoglu, X. Zhang, A. Misra, J. Huang, J. Hirth, Detwinning mechanisms for growth twins in face-centered cubic metals, Acta Mater 58 (6) (2010) 2262–2270.
[43] L. Liu, J. Wang, S. Gong, S. Mao, High resolution transmission electron microscope observation of zero-strain deformation twinning mechanisms in Ag, Phys. Rev. Lett. 106 (17) (2011) 175504.
[44] C.C.T. Zhiming Li, Konda Gokuldoss Pradeep, Dierk Raabe, A TRIP-assisted dual-phase high-entropy alloy: grain size and phase fraction eff ects on de formation behavior, Acta Mater 131 (2017) 323–335.
[45] M. Wang, Z. Li, D. Raabe, In-situ SEM observation of phase transformation and twinning mechanisms in an interstitial high-entropy alloy, Acta Mater 147 (2018) 236–246.
[46] S. Wei, C.C. Tasan, Deformation faulting in a metastable CoCrNiW complex concentrated alloy: a case of negative intrinsic stacking fault energy? Acta Mater 200 (2020) 992–1007.
[47] Y. Chen, D. Chen, X. An, Y. Zhang, Z. Zhou, S. Lu, P. Munroe, S. Zhang, X. Liao, T. Zhu, Unraveling dual-phase transformations in a CrCoNi medium-entropy alloy, Acta Mater (2021) 117112.
[48] P. Yu, R. Feng, J. Du, S. Shinzato, J.P. Chou, B. Chen, Y.C. Lo, P.K. Liaw, S. Ogata, A. Hu, Phase transformation assisted twinning in a face-centered-cubic $FeCrNiCoAl_{0.36}$ high entropy alloy, Acta Mater 181 (2019) 491–500.
[49] K. Ming, X. Bi, J. Wang, Microstructures and deformation mechanisms of $Cr_{26}Mn_{20}Fe_{20}Co_{20}Ni_{14}$ alloys, Mater. Charact. 134 (2017) 194–201.
[50] Y. Bu, Z. Li, J. Liu, H. Wang, D. Raabe, W. Yang, Nonbasal slip systems enable a strong and ductile hexagonal-close-packed high-entropy phase, Phys. Rev. Lett. 122 (7) (2019) 075502.